University of Colorado, Boulder
CU Scholar

Civil Engineering Graduate Theses & Dissertations   Civil, Environmental, and Architectural Engineering

Spring 1-1-2014

Fish Skin: A Thin, Flexible, Protective Membrane

Natasha Elaine Funk
University of Colorado at Boulder, funktasha@gmail.com

Follow this and additional works at: https://scholar.colorado.edu/cven_gradetds

Part of the Biomechanics Commons, and the Mechanics of Materials Commons

Fish Skin: A Thin, Flexible, Protective Membrane

by

Natasha Elaine Funk

A thesis submitted to the

Faculty of the Graduate School of the

University of Colorado in partial fulfillment

of the requirements for the degree of

Master's of Science

Department of Civil, Environmental, and Architectural Engineering

2014

This thesis entitled:
Fish Skin: A Thin, Flexible, Protective Membrane
written by Natasha Elaine Funk
has been approved for the Department of Civil, Environmental, and Architectural Engineering

---

Prof. Franck Vernerey

Prof.Mark Stoykovich

Date _____

The final copy of this thesis has been examined by the signatories, and we find that both the content and the form meet acceptable presentation standards of scholarly work in the above mentioned discipline.

iii

Funk, Natasha Elaine (M.S., Structural Mechanics)

Fish Skin: A Thin, Flexible, Protective Membrane

Thesis directed by Prof. Franck Vernerey

Abstract

Although there have been recent efforts to characterize the important structural character-istics of fish scales and fish skin (e.g., the tensile strength [9] , puncture strength [19], bending rigidity [10]), attempts to fabricate materials that mimic natural fish skins have remained limited. This thesis presents a synthetic fish skin material designed to replicate the structural, dimensional, mechanical, and functional aspects of natural teleost fish skin comprised of leptoid-like scales. The material design and fabrication has been simplified to include (i) a low modulus elastic mesh or dermis layer that holds (ii) relatively (in comparison to the mesh) rigid, plastic scales. While the mesh holds the scales in place even when the skin is deformed, the scales remain free to rotate and interact with neighboring scales or the substrate. The mechanics of the resulting material was quantified, using experiments and theoretical models, in response to in-plane deformations, flexure, and indentation. The mechanical behavior achieved with this design was found to be similar to that of natural fish skin, thus indicating the distinct roles that interacting dermal and scale layers have on the material properties. Overall the synthetic fish skin is flexible and can conformably cover a range of surfaces, including those subject to diverse modes of deformation, making such a material attractive as a low-weight, low-profile protective coating for soft materials.

Acknowledgements

Contents

Section

Figures

Figure

Section 1

Motivation and Overview

1.1   Biological Protective Systems and Engineering

Nature presents innumerable variations in protection systems. From the bony plates on the back of an armadillo to the exoskeletons of crustaceans and the delicate scales on the wings of a butterfly, animals and insects have evolved to defend themselves against predation. In particular, scaled skin provides some of the most effective protection seen for its weight and flexibility. Ancient scaled fish are known to have existed as far back as the Paleozoic period, but their armor consisted of much larger, thicker plates and in more layers than in modern fish [3]. Over time, the need for greater flexibilty and mobility fostered the evolution of these scales into numerous smaller, thinner scales with fewer layers and overall more flexibility, still with outstanding protective characteristics [3]. Today, fish scales are classified into the following groups: placoid, ganoid, cosmoid, and elasmoid (see Figure 1.1) [22].

Placoid scales are typically found on creatures such as sharks, and especially known for their ability to reduce drag, while ganoid scales are the hardest known scales and are the main protection for gars [22],[10]. Elasmoid, or leptoid, scales are further broken down into cycloid and ctenoid type scales, both of which are flexible scales with similar shapes, but cycloid scales sport a smooth surface, while ctenoid scales are found to have numerous small ridges and grooves, creating a rough surface [22],[16]. The structural and mechanical characteristics of these scales are of great interest in engineering biomimetic designs for lightweight protective membranes.

Interestingly, the idea of exploiting the mechanical characteristics and benefits of fish skin is
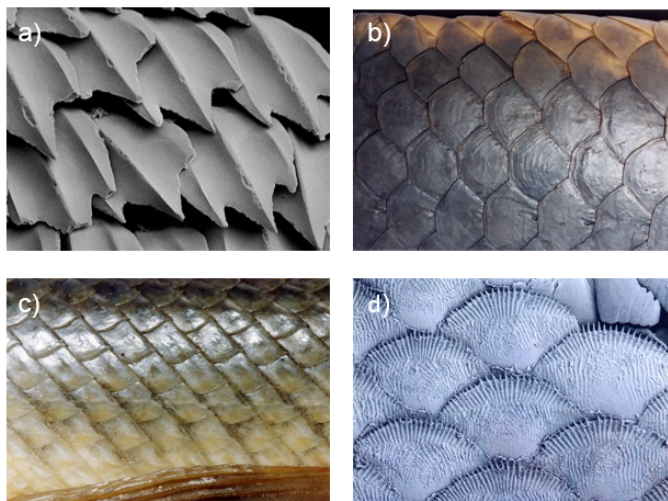
Figure 1.1: Photographs of a) Placoid scales, b) Cosmoid scales of Australian Lungfish, c) Ganoid scales of a Florida Gar, and d) Ctenoid scales (images © Australian Museum, http://australianmuseum.net.au/, Last Accessed April 21, 2014)

not a new one. H. Russell Robinson [13] suggests that perhaps the earliest use of fish armor occurred in the Middle East, where a painting finished sometime around 1411 B.C. depicts a garmet fashioned of bronze scales. Some of the first heavily armored army in the western world were the Sarmatians, who also adopted armors built from metal scale-like shapes, and even used this armor to protect their horses [11]. These ancient people recognized the advantage of fish skin as a flexible alternative to a solid sheet of heavy armor typically depicted for ancient times. Similarly, the Romans preferred scaled armor due to its low cost and ease in fabrication [8]. From the remaining scaled Roman armors existing today, it is surmised that the Romans used a rolling process to create relatively thin sheets from which the scales were cut and punctured with a nail so they could be attached to a base fabric or leather [8]. Figure 1.2 shows a variety of ancient scale shapes used to create such armors.

In modern times, there is still interest in fish scale body armor, but several researchers in the engineering community have also realized the potential for this material as replicable lightweight, flexible armor for use in composite textiles [5], architecture [12],[15], and flexible electronics [19],[7]. These interests have led to increased efforts in understanding the exact mechanical behavior of fish skin, in the hopes for a complete biomimetic "transfer of technology"[24].
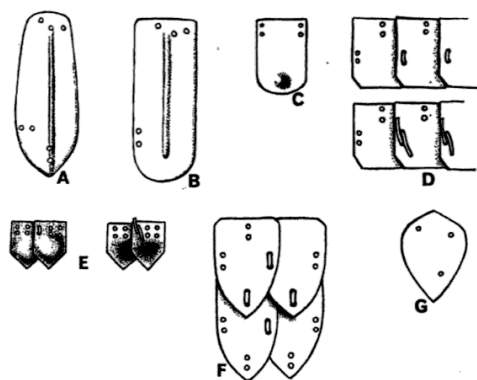
Figure 1.2: Shapes of Ancient Scale Armor a) Egyptian bronze, b) Syrian from Nuzi,c) Egyption with boss, d) Roman bronze, e) Roman bronze, f)Roman bronze, and g)Chinese copper (Image from [13])

1.2   Mechanical Characterization of Fish Skin

Recent efforts to characterize the important structural characteristics of fish scales and fish skin have resulted in a great deal of information on the composition, tensile strength, puncture strength, and flexural rigidity of scales and fish skin. As discussed by Lin, et. al. [9] fish scales display a hierarchical architecture, with a hard, mineralized outer layer and a softer inner lay comprised of collagen fibers arranged in a Bouligand, or plywood-like pattern. This structure provides a unique combination of strength and fracture toughness, which leads to an excellent ability to protect against penetration, while also allowing for flexibility[6]. Zimmerman, et. al. [25] demonstrated with in situ synchrotron small-angle X-ray scattering that during tensile loading, collagen fibers within the scales reorient themselves, giving the scales enhanced ductility and fracture resistance.

In regards to puncture strength, Zhu et. al.[24] characterized the structure and puncture mechanics of the teleost skin from the *M. saxatilis* by examining six different parameters that could affect the puncture resistance of the fish skin. These included substrate stiffness, puncture site (on an individual scale), number of overlapping scales, friction between scales, scale arrangement and overlap, and scale interaction and force dispersal. With these parameters, Zhu, et. al. determined that substrate stiffness was of secondary importance to the mechanics of fish skin during penetration. However, puncture site affected the penetration resistance significantly since the scale of the *M. saxatilis* does not display the same thickness across its surface. As would be expected, more

force was needed to puncture the center region of the scale, which is thicker than the edges of the scale. Perhaps one of the most notable findings in this paper was that puncture force increases almost linearly with the number of overlapping scales, meaning that three scales provide almost three times the penetration resistance of a single scale. This is despite the non-homogeneous structural make-up of the scales. Through the use of finite element modeling, Zhu, et. al. demonstrated that the friction between scales is practically zero, which allows for ease of motion during swimming, but can also be seen as a detriment to puncture resistance, as fully bonded scales would provide more bending stiffness and therefore greater resistance to puncture. The effects of scale arrangement and overlap were considered by penetrating three scales arranged in one of three ways: stacked, staggered overlap (natural arrangement), or rotated. From this test, the researchers noted that the stacked arrangement provided the most resistance to penetration, and that each arrangement allowed for the scales to "sink" into the substrate, and the edges of the scales in the natural arrangement lifted off of the substrate during penetration. These observations led to the last test, which is also of interest in this study - scale interaction and force dispersal. From this test, the researchers observed that the scales reduced the deflection of the substrate during penetration by about 25%, but only in the area near the indenter. Essentially, this demonstrates the scales' role in redistributing the forces from a point load, reducing damage to the underlying substrate [24].

At the macro-scale, or whole fish, level Long et. al. [10] measured the flexural stiffness of the longnose gar *Lepisosteus osseus* during swimming. Flexural stiffness of the gar was measured by gripping a dead specimen in an apparatus that measured applied bending moment as well as curvature of the fish. The flexural stiffness was calculated for the unaltered fish and then compared to the stiffness of the fish after alterations. Specifically, it was shown that cutting the dermis between two caudal scale rows on the gar drastically reduces stiffness, while removing a caudal scale row did not significantly impact the flexural stiffness of the gar beyond the effects of cutting the dermis. These measurements were also performed on live fish, and it was shown that cutting the dermis of the gar reduced tailbeat frequency and propulsive wave speed[10]. This study demonstrated the importance of the dermis with regards to the mechanics of the skin of the gar, specifically with its

contribution to flexural stiffness and swimming efficiency.

These studies discuss just a few of the important characteristics of fish skin discovered over the past few decades, and present a basis for the contributions of this study.

1.3   Background

Even though researchers have made great strides in characterizing real fish skin, attempts to fabricate materials that mimic natural fish skins have remained limited. The main focus of this study is on the replication and characterization of leptoid scale group of the teleost fish, and particularly the flexible properties of individual scales embedded in individual dermal pockets [19].

Ortiz and coworkers [2] explored the effects of scale geometry and composition by creating 21 macroscale prototypes using 3-D printed ABS (acrylonitrile butadiene styrene) scales embedded in a substrate of silicone rubber. It was demonstrated that scale overlap is critical for the distribution of forces across the material, and that it is possible to tailor the overall stiffness of the material by adjusting structural parameters such as the scale overlap, orientation, aspect ratio, and volumetric filling within the substrate [2]. Song [15] and Reichert [12] also developed two separate 3-D printed prototypes based on the armor of *P. senegalus* to better characterize the global and local behavior of this scale type. Specifically, individual scales (local behavior) were printed using a rigid material by the name of Objet VeroWhite to explore the contributions to the mechanical behavior of the skin from (i) peg-and-socket connections between individual scales and (ii) overlapping surfaces. At the global level, Song [15] and Reichart [12] developed helical rings in the image of the overall pattern of scales on the *P. senegalus*. With these models, it was demonstrated that individual scales are important for the overall flexibility of the fish, since an architecture of solid helical rings provided little to no range of motion in comparison to the individual scales. They also demonstrated that the flexible peg-and-socket connections in combination with the sliding, overlapped surfaces were key in *P. senegalus* mobility [15], [12]. On a microsystem level, Kim, et. al. [7], used a transfer printing process to explore two variations of fabrication processes involving scales measuring 600μm x 600μm. In the first variation, scales were attached in an imbricate pattern to molded

poly(dimethylsiloxane) (PDMS) posts using surface hydroxyl condensation reactions. The second variation comprised of transfer printing the scales to a smooth silicon substrate by means of a small PDMS anchor attached to a single edge of the scale [7]. The researchers went on to test the mechanics of these microsystems qualitatively, showing that in both variations, the scales provided full coverage and protection during bending, stretch, and buckling, which is of great interest in the development of flexible electronics. These modern designs and implementations of man-made scaled skins, although sharing structural aspects and duplicating some performance features of natural materials, have not successfully captured key features of the fundamental mechanics in teleost fish skin. Specifically, this study is interested in more flexible armors than those of the *P. senegalus*, in order to characterize the rotational and flexible aspects of individual scales, but unlike the microsystem fabrications, feasibility of construction without advanced technologies was of paramount importance.

1.4 Materials and Fabrication Process

Research into the architecture of fish skin has indicated three components that are key to the mechanical response of fish skin: thin but relatively rigid scales with some degree of overlap (see Figure 1.3), an underlying elastic substrate or dermis, and a periodic distribution of soft, elastic pockets in the substrate into which the scales are inserted [19]. A bio-inspired skin was fabricated, as shown in 1.3c, in a simplified material design from two primary materials (i) dermis layer consisting of a flexible polypropylene mesh or net and (ii) scales of cellulose acetate butyrate (CAB) having an elastic modulus on the order of 7 times larger than that of the mesh as a whole. Individual CAB "scales" were inserted in each opening of the mesh and sewn to the cross-links of the mesh with cotton thread. See Appendix A for further explanation and schematics demonstrating this process.

As in natural fish-skin, the mesh serves the dual purpose of providing a relatively soft, flexible scaffold or backbone for the material, as well as providing a pocket stiffness, which performs the function of allowing rotation of individual scales about the latitudinal axis and restricting rotation about the longitudinal axis. This periodic mesh also controls the scale position and overlap and

thus the scale-scale interactions. At its base, the mesh is a periodically repeated, sinusoidal-shaped, single fiber with E=1300 MPa, a fiber radius of 0.06 ±.01 mm, and with x- and y- dimensions of 5.13±.01 mm and 2.81±.01 mm, respectively, creating diamond-like openings measuring 10.26±.01 mm wide by 5.62±.01 mm tall. The CAB scales, which were attached at the center of each scale to the mesh intersections with cotton thread, provide the protective component of the synthetic material with an elastic modulus of 800 MPa, individual thickness of 0.20±.01 mm, a width of 9.46±.01 mm, a length of 12.68±.01 mm, and a normalized overlapping ratio the ratio of scale spacing to scale length r, of 0.19, which is similar to values typically found in nature - 0.2 to 0.3 [19]. A macroscopic specimen suitable for mechanical characterization was fabricated with an overall area of 153.39±.01 mm in the lateral direction (direction from abdomen-to-dorsal side of the fish, see 1.3c) by 167.87±.01 mm in the longitudinal (from anterior-to-posterior end) direction.

After fabrication, several experimental tests were performed to quantify the mechanics of the resulting synthetic material. The material's response to in-plane deformations, flexure, and indentation were captured and modeled as described on the following pages. The mechanical behavior achieved with this design was found to be similar to that of natural fish skin, thus indicating the distinct roles that interacting dermal and scale layers have on the material properties.
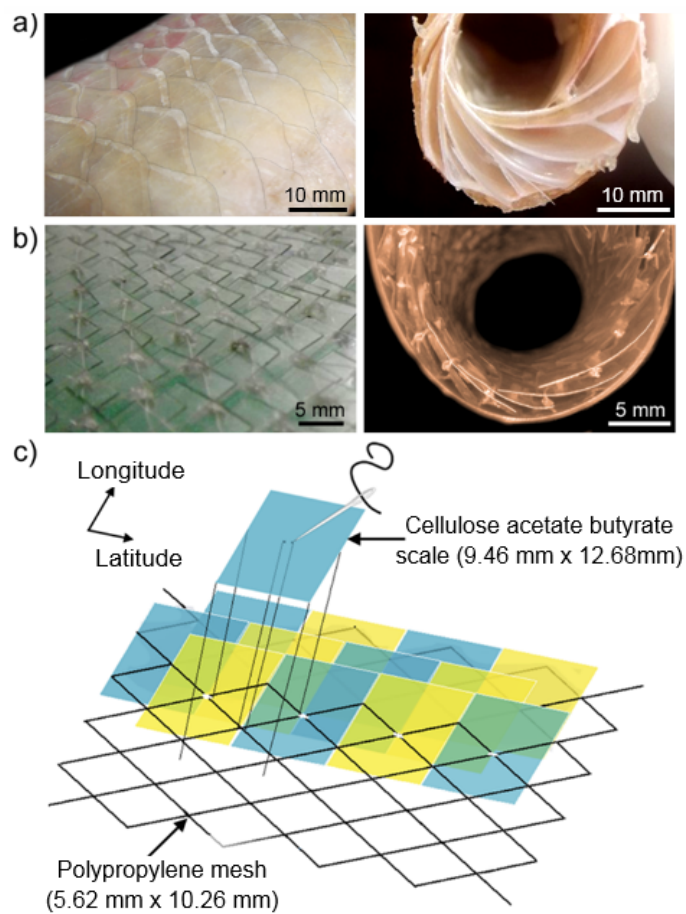
Figure 1.3: Photographs of a) skin from *Mullus surmuletus* and b) the synthetic fish skin when undeformed (left) and under bending deformation (right). c) Schematic of the materials and processes used to fabricate the synthetic fish skin with rigid cellulose acetate butyrate scales and polypropylene fiber mesh.

Section 2

Mechanical Response of Synthetic Fish Skin to In-Plane Deformation

The bio-inspired fish skin's mechanical response to in-plane deformations was first character-ized and modeled as shown in Figure 2.1. The stress-strain response of the fish-skin was compared to two other traditional materials: (i) a single solid sheet of CAB with the same thickness as the scales used for the synthetic material and (ii) the polypropylene fiber mesh without scales. The anisotropic tensile responses of the synthetic fish skin and the mesh were measured in both the longitudinal and the lateral directions as shown by discrete points in 2.1. The data for the solid sheet of CAB is not shown here as deformation was negligible for the range of loading considered. For a full explanation of the testing process, see Appendix A.

2.1   Results

Four notable outcomes resulted from these tests. First, the skin shows a relatively soft response in the longitudinal direction that stiffens with increasing strain. These results demonstrate that in the longitudinal direction, or head-to-tail direction on a fish, the skin is very flexible (much more so than the single, solid scale), allowing for ease in stretching in this direction. Second, this stiffening behavior is controlled primarily by the mesh, the longitudinal response of which is shown in black in Fig. 2.1. As the mesh is placed in tension, deformation initially occurs as bending of the individual fibers, and a very soft response is observed during this regime due to the low bending stiffness of the polypropylene fibers. After a certain point, the fibers begin to carry an increasing amount of uniaxial load, thereby causing a stiffer response to the applied load [20].
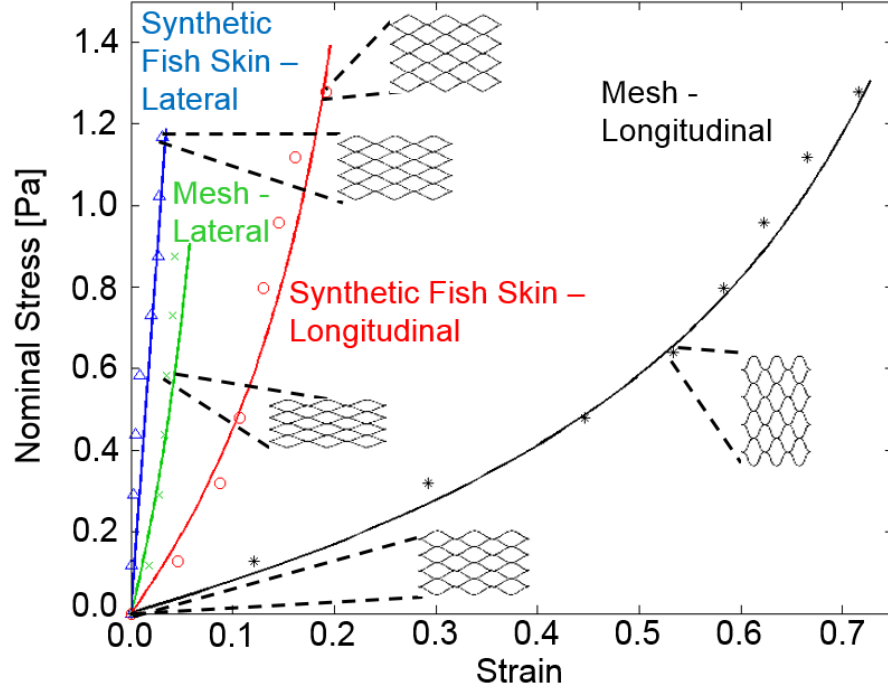
Figure 2.1: Experimental and modeled response of synthetic skin and mesh during in-plane tensile deformation

The third notable observation is provided by comparison of the response in the longitudinal direction of the mesh and the skin, where we see that the scales do increase the stiffness of the material by constraining the displacement of the nodes on the mesh in the lateral direction (or x-direction in Fig. 2.2). Without scales, much larger strains are needed to place the polypropylene fibers in axial tension only, and the individual nodes are almost touching at this point. The scales prevent this nodal movement in the lateral direction, thereby placing the fibers fully in tension at smaller strains and increasing the overall stiffness of the material. This trend holds true for tensile deformation in the lateral direction as well. This trend can be quantified by comparing the Poisson's ratios of the mesh and the skin in the longitudinal and lateral directions (see Fig. 2.2 for strain equations):

$$\nu_{long.,mesh} = \frac{-\epsilon_{trans,long}}{\epsilon_{axial,long}} = .35 \tag{2.1}$$

$$\nu_{lat.,mesh} = \frac{-\epsilon_{trans,lat}}{\epsilon_{axial,lat}} = .26 \tag{2.2}$$

$$\nu_{long.,scales} = \frac{-\epsilon_{trans,long}}{\epsilon_{axial,long}} = .25 \tag{2.3}$$

$$\nu_{lat.,scales} = \frac{-\epsilon_{trans,lat}}{\epsilon_{axial,lat}} = .14 \tag{2.4}$$

These Poisson's ratios demonstrate that the scales are responsible for increasing the stiffness of the material by constraining the mesh in the direction perpendicular to loading. Here, axial strain is the strain computed with respect to the direction of loading, and transverse strain is computed perpendicular to loading - e.g. for the longitudinal test, ϵ_{long} (Fig. 2.2) represents the strain in the axial direction, while ϵ_{lat} (Fig. 2.2) measured during this test represents the strain in the transverse direction. These Poisson's ratios indicate that the scales are responsible for increasing the stiffness of the material by constraining the mesh in the direction perpendicular to loading.

Lastly, the response of the skin under longitudinal loading can be compared to its response under lateral loading. In the longitudinal direction, the scales provide essentially no frictional resistance to axial deformation, since the geometry and fabrication of the skin allows for the scales to slide across each other freely, whereas the scales are restricted from sliding the in lateral direction. Ultimately, these mechanisms allow the mesh to govern the general response of the skin during stretch, dictating that the skin responds more softly in the longitudinal direction than in the lateral direction.

2.2   Model and Discussion

To better understand and verify these mechanisms and their effect on the mechanics of the fish skin material, a simple numerical model for the in-plane deformation of an elastic mesh with and without scales was developed. An idealized mesh (bottom inset in Fig. 2.1a) was created to model the experimental results of the mesh and synthetic fish skin. As an idealized geometry, the modeled geometry does not exactly match the geometry of the actual mesh, which is more complicated. Nevertheless, the geometry displays the same overall diamond-like openings bounded by sinusoidal-shaped fibers, modeled as $y = ax - bx^3$. The geometry of the mesh was determined by the numerical implementation of a finite element model for large beam deformation [17] (details of this model provided in Appendix B)and the stress-strain response was computed by imposing

periodic boundary conditions on the element as shown in Figure 2.2.
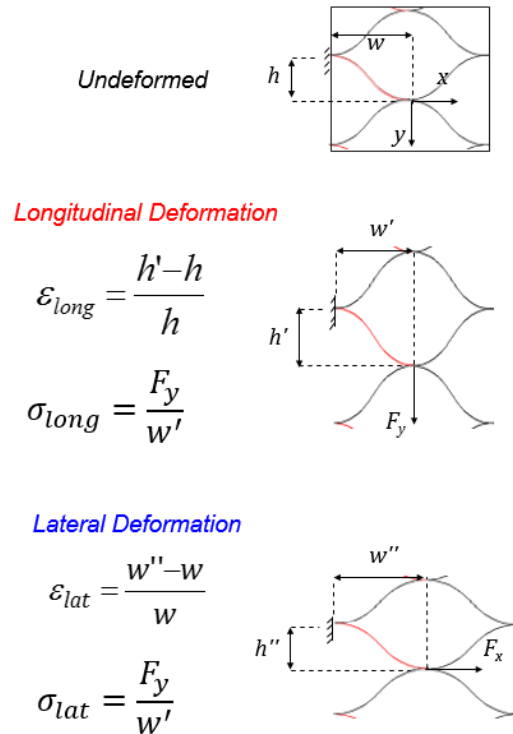
Figure 2.2: Free-body diagram of periodic cell used to model axial loading responses. Stress is calculated as $\sigma_x = \frac{F_x}{h'}$ or $\sigma_y = \frac{F_y}{w'}$, respectively.
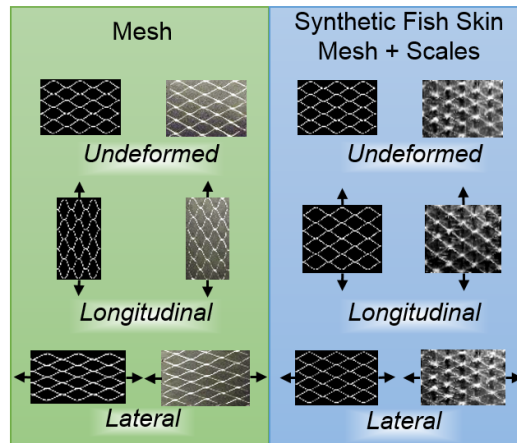
Figure 2.3: Comparison between Model and Actual Results from In-plane Deformation - modeled geometry on the left in each frame

This concept was extended to model stress-strain response of the skin by idealizing each scale as a spring separating the nodes of the mesh in the lateral direction. Essentially, by placing a displacement control on these nodes at each loading increment, the fibers of the mesh are forced
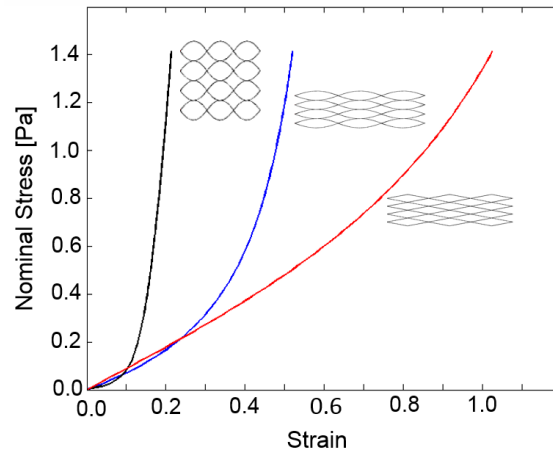
Figure 2.4: Comparison between Model and Actual Results from In-plane Deformation - modeled geometry on the left in each frame

into uniaxial loading sooner than when the nodes are allowed to move freely, thus increasing the tensile stiffness of the modeled material, and reducing the Poisson's ratio. Figure 2.3 demonstrates the modeled geometry in comparison to the actual mesh geometry. Figure 2.4 demonstrates the utility of the proposed model for designing a mesh or dermis layer with the desired tensile response for the synthetic fish skin material. Three distinct mesh geometries with identical fiber dimensions and physical properties are considered here and exhibit different mechanical responses; conceivably any number of mesh geometries could be considered to achieve an optimal balance between skin flexibility and stiffness. Not shown in this figure is the effect of mesh geometry in the lateral direction, but that is simply because the results are similar in that different geometries can be created to produce different stress-strain responses. In design, both directions would be considered. It may even be of interest to researchers to optimize a mesh such that it was isotropic. This would not only lead to greater ease in characterizing the material, but it would also lend itself more favorably to body armor, as flexibility in both directions can be equally important.

Section 3

Mechanical Response of Synthetic Fish Skin to Flexure

The presence of scales on the skin becomes a salient feature of fish-skin mechanics during out-of-plane deformation as we will see in the context of skin bending and indentation by a sharp object. For example, the relatively high curvatures of the skin achieved during swimming serves a mechanical function to fish, as it acts as a spring to restore elastic energy and assist in more efficient propulsion. [10],[19]. Imbricate scales also are important as protection when the fish skin is subjected to extreme surface instabilities such as wrinkling of the skin (from pinching and/or buckling) or indentation. In this context, the synthetic fish skin's response to flexure was measured in two directions - bending about the lateral axis and bending about the longitudinal axis . The load-displacement responses in Figure 3.1 of the fish skin were compared to flexure of an unscaled, foam substrate (i.e., analogous to the flesh of a fish). Loads were applied incrementally at the center of each specimen, and deflections were measured at the loading point (using the testing setup illustrated in Appendix A, Figure A.3). The procedure used to determine the flexural response is detailed in Appendix A. Figure 3.1 demonstrates that the synthetic skin behaves similarly to real skin in that it increases the overall flexural stiffness of the foam substrate. In fact, it was seen during testing that at the maximum load, the unscaled foam specimen displayed potentially critical curvatures (as indicated by a kink at the point of loading), whereas the same foam substrate, when protected by the synthetic fish skin, displayed much smaller curvatures.

3.1   Results

From the mechanical characterization of the bio-inspired skin's flexural response, the following conclusions were drawn about the mechanical behavior of the skin during flexure. First, the skin behaves softly in the longitudinal direction (bending about the lateral axis) in comparison to a solid sheet of CAB with equal thickness (36 mm of deflection at a maximum load of 1 N in comparison to 21 mm of deflection at the same load). Results from the flexural response of the solid CAB are not shown here for clarity. The mechanism controlling this soft behavior is the small rotational stiffness of the scale pockets, which allows for large scale rotation rather than individual scale bending under relatively low applied moments. At larger bending moments, however, the skin stiffened significantly as the curvature increased and scale-scale interactions lead to the bending of each individual scale. Figures 1.3a and 1.3b demonstrate that that in flexure, both the real and synthetic fish scales exhibit rotational and bending properties, just like those shown in Figure B.4. In the lateral direction (bending about the longitudinal, or head to tail, axis), it was discovered that
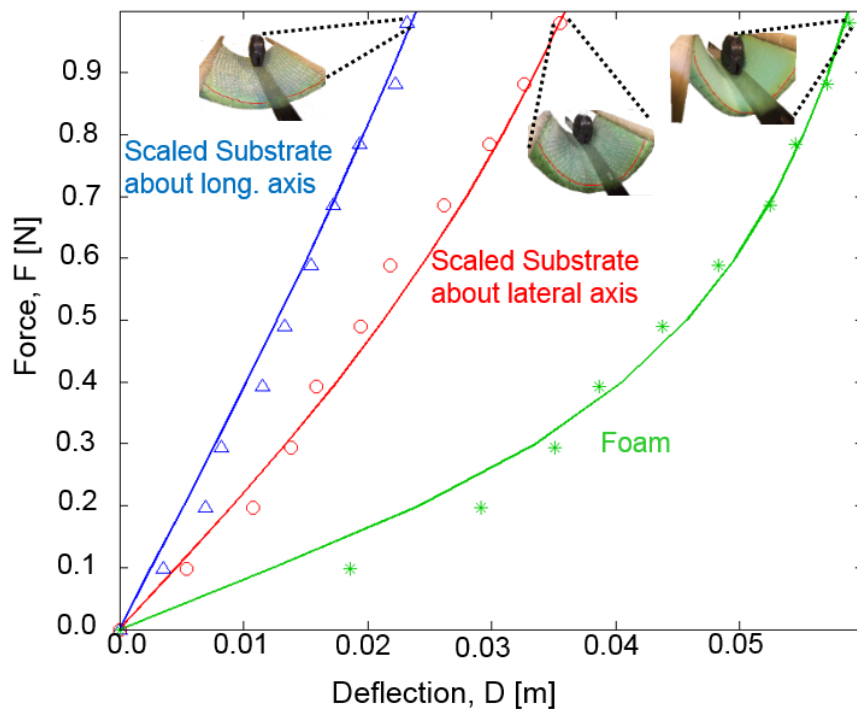

Figure 3.1: Experimental and modeled flexural response of specimen under uniaxial bending. Experimental results shown as discrete points, and modeled as solid curves.

the skin responded more softly than a solid sheet of CAB with equal thickness attached completely to the top of the foam specimen, which can be explained by the discontinuity of material across the surface of the skin. Contrary to the behavior in the longitudinal direction, however, the limitation on scale rotation in the lateral direction restricts overall bending of the skin in this direction, leading to a stiffer response and eliminating the stiffening behavior seen in the longitudinal direction . This stiffer behavior can also be attributed to the fact that the flexural stiffness of a single scale, EI_s, is larger about the longitudinal axis since the scales are longer and $I_s = lh^3/12$.

3.2 Model and Discussion

In order to verify the assumptions in regards to the mechanisms controlling the skin's response to bending, a numerical model was developed based on the derivations of Vernerey and Barthelat [19] that could qualitatively predict the behavior of the skin in terms of the mechanical properties, spatial organization, and morphometry of individual scales. Three separate models were needed to compute the flexural stiffness for each test specimen, one each for the foam only, scales bending about the longitudinal axis, and scales bending about the lateral axis. Exact details of these models are described in Appendix B, and the results are shown as solid lines in Figure 3.1.

As indicated in Figure 3.1, the proposed model conforms well to the experimental results, indicating that this model has potential for the design and optimization of synthetic scaled skins. In Fig. 3.2, the model is extended to explore two approaches that may be used to influence the skins bending response in the longitudinal direction: (i) tuning pocket stiffness and (ii) controlling substrate thickness. The effect of pocket stiffness is considered by removing the foam stiffness from the model (specifically achieved by setting $t_{foam} = 0$). These results are shown as solid curves in Figure 3.2, where it is should be noted that an increase in normalized pocket stiffness, $\bar{K}$, leads to an increase in skin stiffness and a reduction of the stiffening response at higher curvatures. The blue curve ($\bar{K} = 0.05$, far right) demonstrates the effect of low pocket stiffness, which causes the overall skin to be much more flexible initially than a similar specimen with high pocket stiffness. The discrete points in Fig. 3.2 represent the scaled substrate as modeled in Fig. 3.1, only with varying
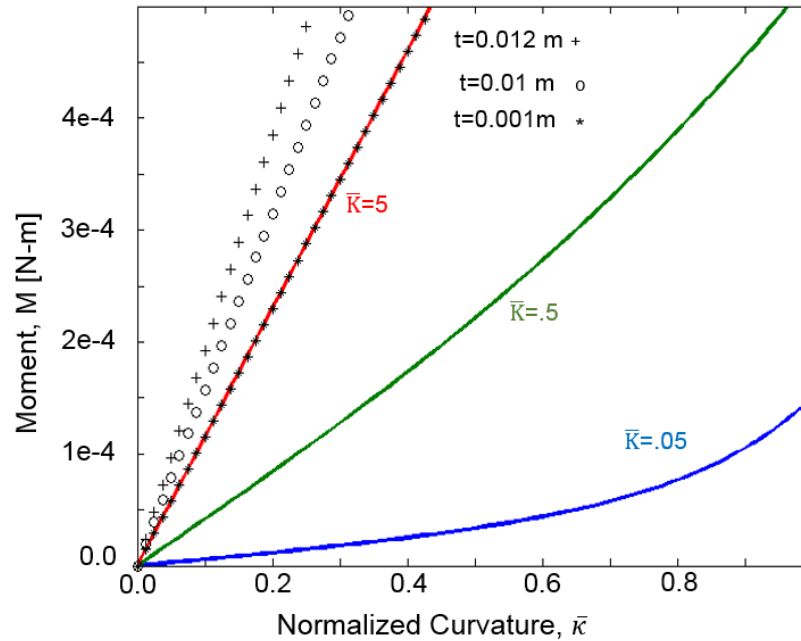
Figure 3.2: Effect of the normalized pocket stiffness, $\bar{K} = \frac{Kl}{EI_s}$, and substrate thickness on the moment/curvature response of the skin.

values of substrate thickness as specified within the plot. It is noteworthy that adding the foam substrate to the model increases the stiffness of the specimen such that the pocket stiffness no longer has an effect on the overall response of the skin. It is also observed that decreasing the thickness of the foam substrate decreases the stiffness of the specimen. With this type of modeling capability, it would be possible to customize the response of the synthetic skin based on the potential use of the material. For instance, it may be of interest to researchers to develop a material that was almost equal in flexibility about both axes of the skin to ensure property flexibility in any direction. Here a base set of parameters is provided, which can be optimized to achieve such results.

Section 4

Mechanical Response of Synthetic Fish Skin to Indentation

Perhaps the most important function of fish skin is its resistance to penetration [24],[22]. The same variables that control the skin's response in flexure also influence its response during indentation [20]. The main characteristic controlling the indentation response, however, is the imbricate pattern of the scales. This overlapping allows for the transfer of forces from a single scale to the scales directly adjacent, dispersing the force and ultimately decreasing damage to underlying tissues. Zhu et. al. [24] performed indentation tests on M. saxatilis specimen using a sharp needle (35 μm tip), demonstrating that scaled skin was able to resist about three times the penetration force compared to unscaled skin, and under blunt loading (probe diameter of 2.2 mm), the scales reduce absolute deflection by interlocking redistributing the force across the skin.

4.1   Results

In this study, indentation tests were performed on the synthetic fish skin, a solid sheet of CAB (two layers of CAB in the same dimension of the scaled specimen), and an unscaled foam specimen with a cylindrical indenter of radius 1.14 mm (see Appendix A for detailed experimental procedures). As Figures 4.1 shows, the synthetic skin behaves in the same manner as the M. saxatilis specimen with regards to increased penetration resistance compared to the unscaled specimen, and as establish earlier in the thesis, the scales have the added benefit of flexibility (soft responses in tension and bending), unlike the solid sheet of CAB. Figure 4.1 also demonstrates that approximately the same amount of energy is needed to penetrate the synthetic fish skin and

the solid sheet of CAB, with one important caveat. The fish skin displays greater deformation at lower forces, indicating that it takes less energy to flex and stretch the skin which demonstrates that the skin is more flexible than a solid sheet of CAB, while providing approximately the same energetic resistance to a penetration force. To further quantify the skin's resistance to penetra-
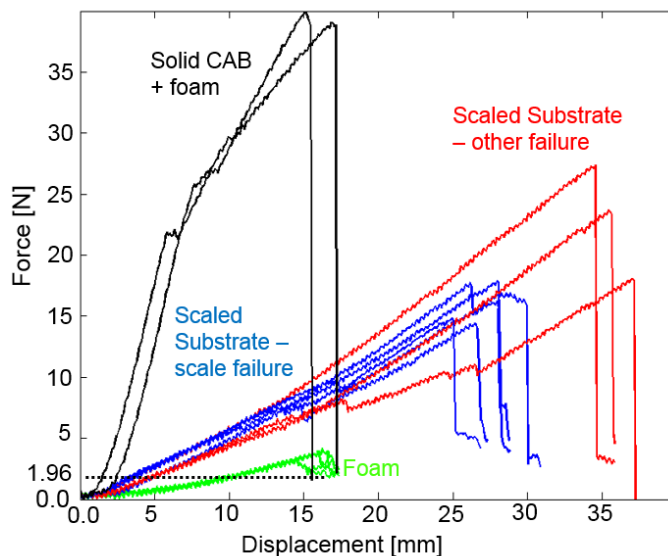
Figure 4.1: Effect of scales on resistance to puncture. Scale failure indicates direct puncture of a scale, while other failure indicates a failure of the synthetic material either failure of the mesh or buckling of a scale.

tion and the mechanisms that allow this behavior, the three specimen were indented at a static load of 1.96 N (the critical load for the unscaled foam specimen) and the surface contours were measured and plotted in Figure 4.2. From the results in Figure 4.2, we ascertain that the scales prevent unstable localized deformation by dispersing the applied force over a larger area. This behavior is contributed to by the nonlinear bending mechanisms described earlier in the thesis, and is a function of individual scale size [4]. At first, the scale or scales directly in contact with the indenter transfer this force to surrounding scales through scale rotation. As the force increases, localized curvature increases, and just as in the case of bending, individual scales begin to bend and stiffen the response of the material. It is also important to be cognizant of the fact that force dispersion relies directly on the size of the scales i.e. larger scales will promote force dispersion over larger areas, while smaller scales will be associated with a smaller area of dispersion. This

effect is demonstrated in Figure 4.2. If we consider the solid CAB to be a very large scale, we see that it disperses the force over a much larger area than the synthetic skin. Likewise, if we were to imagine that the scale size was infinitely small, we would see a response similar to that of the unscaled foam substrate, which disperses the force over a very small area, creating a situation that is prone to early damage nucleation in the substrate. The choice of scale size is a parameter that can be tailored to achieve the desired response of the skin during indentation, as a direct trade between protection and flexibility.
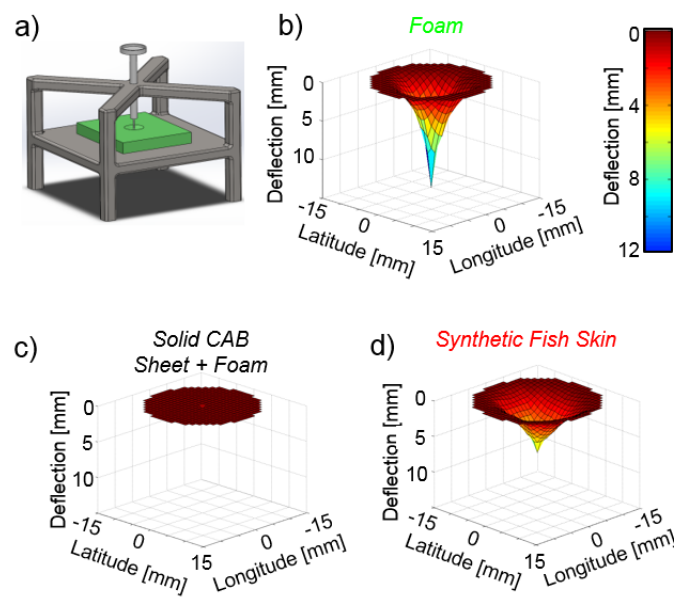
Figure 4.2: a)Schematic of test set-up and b)-d) contour plots of the specimen surface under a load of 1.96 N (critical load for foam only scenario).

4.2   Discussion

At this time, a comprehensive indentation model for scaled skins does not exist. This is left as future work in the attempt to fully characterize the structural mechanics of fish skin. There are, however, a couple of base models show the potential for expansion into a bending model. In particular, the bending model proposed by Vernerey and Barthelat [19] used in this study certainly has potential in being expanded to encompass bending in three-dimensions, which is the essential behavior during indentation. As noted throughout this study, the scales on the fish skin disperse

forces by interlocking, rotating, and finally bending which ultimately relieves the instability created by a single point load. Vernerey, et. al. [21] have developed a computational approach in order to determine the influence of the microstructure - scales, pocket stiffness, etc. - on the overall behavior of the skin by homogenizing the skin based on a representative volume element (RVE). With this approach, they determined that it is feasible to model the scales as Kirchhoff plate structures, and by imposing periodic boundary conditions around the RVE, the response of the skin during bending can be predicted [21]. It is not implausible to think that a model such as this could extend into predictions regarding the skin's response to indentation.

As for this study, a couple of notable control parameters identified by the penetration test are parameters of interest for furthering the future fabrication of biomimetic fish skin. These parameters, as identified in Figure 4.1 were general fabrication technique and material strengths. It was found here that two failure modes are possible for the synthetic skin during indentation: scale failure and other failure. Scale failure indicates the occurrence when a single scale was punctured by the indenter, and can be modified by choosing a stronger material, or by increasing the thickness of the individual scales. Other failure indicates the failure of the mesh a break in the fiber of the mesh or scale buckling, when a scale folded upon itself and fell through the mesh. This failure mechanism can be avoided by selecting a stronger mesh, increasing the overlap of the scales (to prevent fall-through), or increasing the flexural strength of the scales. Even with these imperfections, the synthetic fish skin displays a very similar behavior under indentation as real fish skin as shown by Zhu et. al. [24], in that it is able to withstand much larger loads than the foam specimen on its own by magnitudes (about 7 times the failure load of the foam specimen at its weakest point).

Section 5

Conclusions

In summary, this study proposes a simple fabrication procedure for creating biomimetic fish skin. By characterizing the behavior of this material during in-plane deformation, flexure, and indentation, it is shown that this synthetic fish skin behaves in a similar manner to real fish skin, indicating its potential for providing the unique and desired combination of flexibility and protection found in real fish skin. The novelty of this process lies in the fact that no expensive machinery or materials were needed to create a stand-alone biomimetic protective material that can be attached to a variety of substrates. With this simple process this study shows that, just as is seen in real fish skin, overlap, underlying mesh geometry, and material strength contribute significantly to the mechanical behavior of synthetic fish skin, and are all important parameters to consider in future development of synthetic fish skin.

Future recommendations for furthering the design of protective synthetic fish skin include the development of a model to more accurately predict the skin's response to indentation. Penetration resistance is of utmost importance, particularly in regards to the application of fish skin as body armor, and a model to optimize the flexibility, weight, and penetration resistance of a material is paramount for the development and application of said materials.

Bibliography

[1] Ashley Browning. Mechanics ad Design of Flexible Composite Fish Armor. PhD thesis, MAssachusetts Institute of Technology, 2012.

[2] Ashley Browning, Christine Ortiz, and Mary C Boyce. Mechanics of composite elasmoid fish scale assemblies and their bioinspired analogues. Journal of the mechanical behavior of biomedical materials, 19:75–86, 2013.

[3] Benjamin JF Bruet, Juha Song, Mary C Boyce, and Christine Ortiz. Materials design principles of ancient fish armour. Nature materials, 7(9):748–756, 2008.

[4] Po-Yu Chen, Jeffrey Schirer, Amanda Simpson, Richard Nay, Yen-Shan Lin, Wen Yang, Maria I Lopez, Jianan Li, Eugene A Olevsky, and Marc A Meyers. Predation versus protection: fish teeth and scales evaluated by nanoindentation. Journal of Materials Research, 27(1):100, 2012.

[5] L. Hatjasalo and K. Rinko. Elastic composite structure, 2006. US Patent 7,153,789.

[6] Toshiyuki Ikoma, Hisatoshi Kobayashi, Junzo Tanaka, Dominic Walsh, and Stephen Mann. Microstructure, mechanical, and biomimetic properties of fish scales from pagrus major. Journal of Structural Biology, 142(3):327–333, 2003.

[7] Seok Kim, Yewang Su, Agustin Mihi, Seungwoo Lee, Zhuangjian Liu, Tanmay K Bhandakkar, Jian Wu, Joseph B Geddes, Harley T Johnson, Yongwei Zhang, et al. Imbricate scales as a design construct for microsystem technologies. small, 8(6):901–906, 2012.

[8] Roy Laible. Ballistic materials and penetration mechanics, volume 5. Elsevier, 2012.

[9] Y.S. Lin, C.T. Wei, E.A. Olevsky, and Marc A. Meyers. Mechanical properties and the laminate structure of arapaima gigas scales. Journal of the Mechanical Behavior of Biomedical Materials, 4(7):1145 – 1156, 2011.

[10] J Long, M Hale, M Mchenry, and M Westneat. Functions of fish skin: flexural stiffness and steady swimming of longnose gar, lepisosteus osseus. The Journal of experimental biology, 199(10):2139–2151, 1996.

[11] Helmut Nickel. The dawn of chivalry. The Metropolitan Museum of Art Bulletin, 32(5):pp. 150–152, 1973.

[12] Steffen Heinz Reichert. Reverse engineering nature: design principles for flexible protection inspired by ancient fish armor of Polypteridae. PhD thesis, Massachusetts Institute of Technology, 2010.

[13] H Russell Robinson. Oriental armour. Courier Dover Publications, 2013.

[14] M Schrodt, G Benderoth, A Kuhhorn, and G Silber. Hyperelastic description of polymer soft foams at finite deformations. Technische Mechanik, 25(3-4):162–173, 2005.

[15] Juha Song. Multiscale materials design of natural exoskeletons: fish armor. PhD thesis, Massachusetts Institute of Technology, 2011.

[16] Seiichi Sudo, Koji Tsuyuki, Yoshiyasu Ito, and Toshiaki Ikohagi. A study on the surface shape of fish scales. JSME international journal. Series C, Mechanical systems, machine elements and manufacturing, 45(4):1100–1105, 2002.

[17] F. Vernerey and R. Pak. Analysis of soft fibers with kinematic constraints and cross-links by finite deformation beam theory. Journal of Engineering Mechanics, 137(8):527–536, 2011.

[18] Franck J Vernerey and Francois Barthelat. On the mechanics of fishscale structures. International Journal of Solids and Structures, 47(17):2268–2275, 2010.

[19] Franck J. Vernerey and Francois Barthelat. Skin and scales of teleost fish: Simple structure but high performance and multiple functions. Journal of the Mechanics and Physics of Solids, 68(0):66 – 76, 2014.

[20] Franck J. Vernerey and Francois Barthelat. Skin and scales of teleost fish: simple structure but high performance and multiple functions. Journal of the Mechanics and Physics of Solids, accepted for publication, 2014.

[21] Franck J. Vernerey, Kamtornkiat Musiket, and Francois Barthelat. Mechanics of fish skin: A computational approach for bio-inspired flexible composites. International Journal of Solids and Structures, 51(1):274 – 283, 2014.

[22] Wen Yang, Irene H Chen, Bernd Gludovatz, Elizabeth A Zimmermann, Robert O Ritchie, and Marc A Meyers. Natural flexible dermal armor. Advanced Materials, 25(1):31–48, 2013.

[23] Deju Zhu, Cesar Fuentes Ortega, Ramak Motamedi, Lawrence Szewciw, Franck Vernerey, and Francois Barthelat. Structure and mechanical performance of a modern fish scale. Advanced Engineering Materials, 14(4):B185–B194, 2012.

[24] Deju Zhu, Lawrence Szewciw, Franck Vernerey, and Francois Barthelat. Puncture resistance of the scaled skin from striped bass: Collective mechanisms and inspiration for new flexible armor designs. Journal of the mechanical behavior of biomedical materials, 24:30–40, 2013.

[25] Elizabeth A Zimmermann, Bernd Gludovatz, Eric Schaible, Neil KN Dave, Wen Yang, Marc A Meyers, and Robert O Ritchie. Mechanical adaptability of the bouligand-type structure in natural dermal armour. Nature communications, 4, 2013.

Appendix A

Methods and Materials

A.1   Fabrication

CAB was purchased as a 90 mm x 60 mm sheet, and then cut into small rectangles measuring 9.8 mm x 12.5 mm. The width of each rectangle was controlled by the dimensions of the available mesh. After each scale was created, two small adjacent holes were punched into the center of the scale in preparation for fastening, via sewing needle and thread, each scale to the mesh. Once prepared, a scale was inserted through an opening the mesh so that one half of the scale lay on top of mesh, and the other half lay under the mesh. The pre-made holes were aligned with the mesh node corresponding to the opening, and cotton thread was used to tack the scale to the node with three stitches and a single knot. This process was repeated for each node on the mesh. Figure A.1 demonstrates this process.
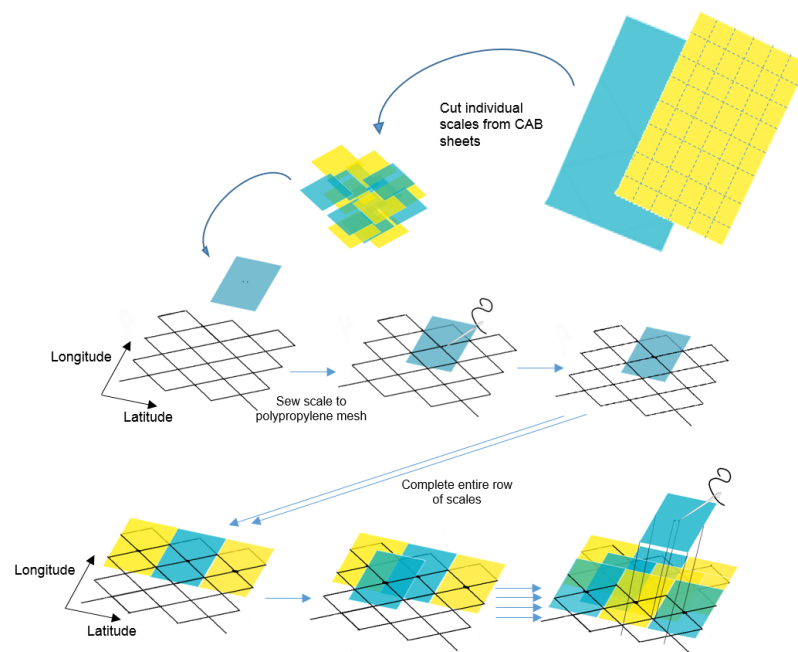
Figure A.1: Schematic of the fabrication process

A.2   In-plane Testing

Tensile tests were performed on three separate materials: the polypropylene mesh, the synthetic fish skin, and the double layer of CAB. During testing, the upper end of the specimen was attached to a smooth metal rod every 10 mm along the edge of the material. The free end was then attached to a smooth metal rod in the same manner. The upper rod was then placed between two supporting beams near a smooth, vertical surface to reduce any out-of-plane deformation. Loading
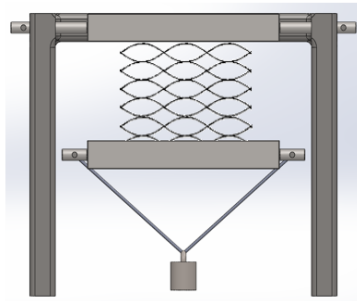
Figure A.2: Schematic of test set-up used to determine in-plane tensile response of mesh and skin

was then performed manually in increments of .2 N, and deflection was measured at the center point of the specimen after the application of each load. Deflection was measured only after the specimen reached equilibrium, and care was taken to prevent the mesh from interacting with the vertical surface at back. Once this process was completed for the specimen in one direction (e.g. longitudinal) the metal roads were then attached to the perpendicular sides and the same specimen was tested in the opposite direction.

A.3   3-point Bending Test for Flexural Response

Flexural response of three different specimen was determined by attaching the two sides of the specimen opposite one another to wooden rods at every $10\pm.01$ mm along the material sides. These rods were then laid on parallel supporting beams which allowed the rods to freely move closer to one another as a line load was applied parallel to the wooden rods, directly in the center of the specimen. After a load was applied, the specimen was allowed to settle before a deflection measurement was taken at the point of loading. Loads were applied manually in increments of 0.1

N. Once a specimen was tested in flexure about one axis, the wooden rods were attached to the perpendicular sides, and the specimen was tested again in the same manner. For those specimen consisting of two materials, i.e. the scaled foam and solid CAB plus foam specimen, the protective material was attached to the foam using stitches of cotton thread at every 10±.01 mm along the edges of the foam. No attachments were made within the center portion of the foam.
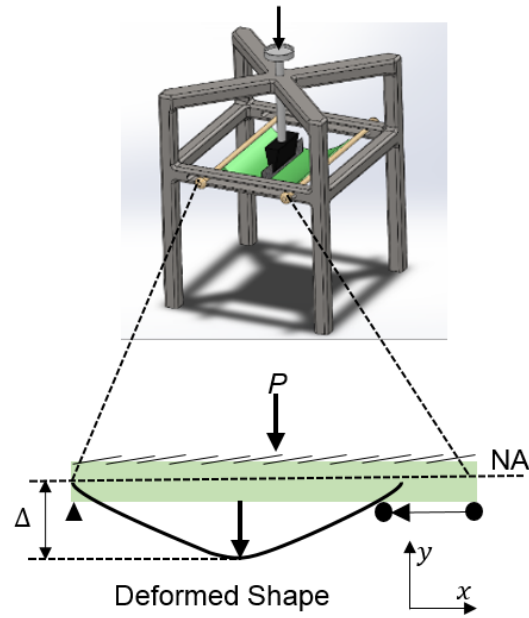
Figure A.3: Schematic of flexural test set-up and measured quantities for flexural tests

For the sake of developing a numerical model that could replicate these results, it was also necessary to measure the compressive and tensile moduli of the open-celled polyurethane foam specimen. The tensile modulus of elasticity was determined by first attaching one metal rod to each of the shorter ends (153.39±.01 mm x 11.99±.01 mm) of the foam specimen with cotton thread stitches at every 10±.01 mm along the edge of the specimen. Then the ends of one rod were place upon two parallel supports and the other end of the specimen was allowed to hang freely. The free end of the specimen was then loaded manually with four different loads, and the tensile deformation was measured at the center of the specimen after the loaded specimen reach equilibrium. This process was repeated three times, and a stress-strain curve was created to determine the modulus of elasticity for each test. The modulus was determined by the slope of a linear trendline fit to the experimental results. The moduli of each test were averaged to

determine the final tensile modulus of elasticity of .06 MPa. Unlike the tensile modulus, it was much more difficult to obtain the compressive modulus. In compression, open-celled foam behaves in a non-linear fashion due to the difference in material properties between the individual fibers of the foam and the foam as a whole. Figure A.4 shows the typical response of open-celled foam
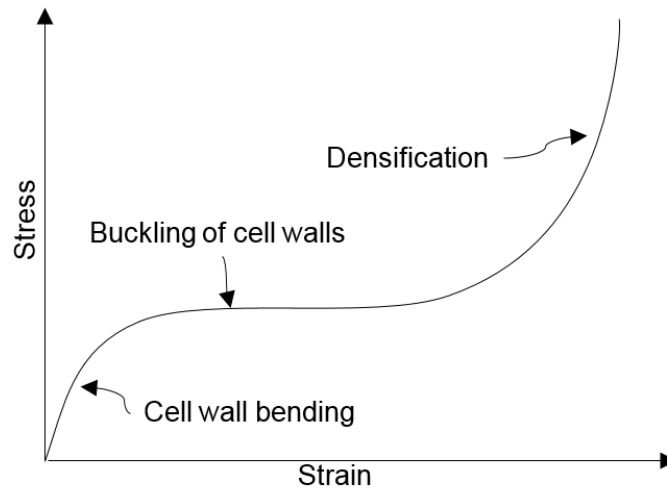
Figure A.4: Generalized stress/strain response of open-celled foam under compressive loading during compression [14]. When the specimen is first loaded, the response of the material is that of the cell wall bending, where a cell is considered to be one of the thousands of small bubbles within the foam. As the load is increased, these walls become unstable and buckle, drastically reducing the stiffness of the material. If loading is continued, all of the vertical components of the fibers within the foam have buckled, and the material exhibits a strain stiffening response as the fibers act more like a homogenous material made only of solid polyurethane[14]. In this report, the main response under consideration was that of the cell wall bending, since the compressive loads seen by the foam during flexure were assumed to remain within this linear region. In order to measure the compressive modulus, a small foam specimen measuring 43.89±.01 mm long by 41.92±.01 mm wide by 73.53±.01 mm thick was placed in compression by applying a surface load to the top of the specimen and measuring the deflection. A total of six different loads were applied to the specimen, and the specimen was allowed to fully settle before deformation measurements were taken at the center of the long edge of the specimen. These data points were then fit with a linear trend line,

and the compressive modulus was taken as the slope of said trend line - .2 MPa.

Lastly, it was necessary to experimentally determine the modulus of elasticity of the CAB for the purposes of calculating the flexural stiffness of the scales and solid sheet of CAB. This was accomplished by performing tensile tests on CAB specimen with small widths (3.44±.01 mm and 4.20±.01 mm) and respective lengths of 52.81±.01 mm and 152.62±.01 mm. During testing, the top portion of the specimen was fixed, and a tensile load was manually applied downward in discrete increments. After each load was applied, the displacement of the bottom end of the specimen was measured. With this data, the stress and stress were calculated and plotted to find the average modulus of elasticity of 800 MPa as the slope of the stress-strain curve.

A.4   Indentation

The first indentation test performed on each specimen involved the indentation of each specimen using a 1.14 mm in diameter indenter and a static load of 1.96 N. This load was chosen because it is just below the critical load for the foam specimen. For each specimen, this static indentation test was performed three times. Each time, the load was applied to the specimen at least 30 mm away from the edge of the specimen to avoid effects from the boundaries of the specimen. Fourteen to fifteen deflection measurements were taken at one millimeter intervals from the origin, or indentation point, in a radial pattern of every 30°, giving a total of 168 measurements for each test(see Fig. A.5). In the case of the foam specimen and the solid CAB plus foam specimen, the deflection from indentation was determined to be symmetrical about all axes, so all of the measurements were averaged for plotting the contours seen in Figure 4.2. The scaled specimen showed symmetry about the longitudinal direction, so the measurements were average across both sides of the specimen for plotting.

Figure A.5: Diagram of measurements taken for static indentation test

Penetration testing with the Instron machine was the last

round of testing, as it was destructive. Just like the static indentation tests, the specimen were indented with a 1.14 mm diameter indenter at a rate of .1 mm/s until failure. The effects of loading rate were not considered in this study. Direct measurements from the Instron device were plotted in Figure 4.1. Effects of loading rate were not considered for the purposes of this thesis

Appendix B

Supplementary Information

B.1　Finite Deformation Beam Theory - In-plane Stress/Strain Response Model

The stress/strain response of the mesh during tensile loading was calculated using the finite deformation beam theory developed by Vernerey and Pak [17]. Taking note of the periodic geometry of the mesh, the response of the mesh was determined numerically by placing kinematic boundary conditions on a single polypropylene fiber as shown in Figure 2.2 and computing the conjugate forces. The modeled fiber, or beam, had an elastic modulus of 1300 MPa and a circular cross-section with a radius of 0.21 ± 0.01 mm. Shear effects were neglected since the beam was very long in comparison to its thickness. The undeformed geometry of the beam (as shown in red in Figure 2.2) along its length as modeled as a cubic function: $y = .75x - 4x^3$. In order to implement Vernerey and Paks model on this unit cell, the beam was divided into 40 finite elements. At each increment of loading, the stress on the fiber was calculated as the applied force divided by the effective mesh width w (longitudinal deformation) or length l (lateral deformation) as denoted in Figure 2.2:

$$\sigma_{long} = \frac{F_y}{w'} \tag{B.1}$$

$$\sigma_{lat} = \frac{F_x}{h''} \tag{B.2}$$

Similarly, the strain was computed by dividing the change in effective mesh length or width by the undeformed length, l (longitudinal deformation) or width, w (lateral deformation). This method of computing stresses and strains effectively normalized the response of the mesh by the unit cell shown in Figure 2.2, which allowed for a direct comparison between the model and the experimental results as in Figure 2.1. The following is a detailed explanation of the model used. For more in-depth information regarding this theory, please see *Analysis of Soft Fibers with Kinematic Constraints and Cross-Links by Finite Deformation Beam Theory* by Franck Vernerey and Ronald Pak [17].

In the field of bioengineering, the ability to model the deformations of thin fibers during tension, compression, and flexure is key to developing materials with desired characteristics for protection, flexibility, durability, and many other characteristics. For this reason (and others) Vernerey and Pak [17] successfully solved the problem of finite deformation of single or multiple fibers with imposed kinematic constraints with the use of a hybrid analytical/numerical method. The following is a summary of this theory, including the governing equations, reductions of said equations, and the kinematic constraints proposed in their theory.

Kinematics, equilibrium equations, boundary conditions, and constitutive relations are integral for the development of the finite deformation beam theory. Figure B.1, copied from *Analysis of Soft Fibers with Kinematic Constraints and Cross-Links by Finite Deformation Beam Theory* [17], shows the free-body diagram used to describe the physical set-up used for this theory. From Figure B.1, the following quantities can be defined:

$$\text{Shear deformation}, \alpha = \phi - \beta \tag{B.3}$$

$$\mathbf{X}' = \begin{bmatrix} \cos \phi_0(s) \\ \sin \phi_0(s) \end{bmatrix} \tag{B.4}$$

and

$$\mathbf{x}' = (1 + e) \begin{bmatrix} \cos \beta(s) \\ \sin \beta(s) \end{bmatrix} \tag{B.5}$$
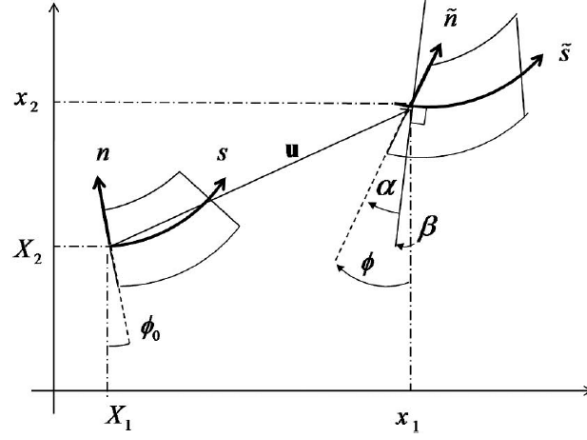
Figure B.1: Free-body diagram of beam element used in the finite deformation beam theory.

where e is the strain, giving the current length of a differential beam segment as $(1 + e)ds$, $\mathbf{X}$ gives the initial coordinates of the beam, $\mathbf{x}$ gives the coordinates of the beam in its deformed state, and the prime notation indicates the derivative of these items with respect to the centroidal curvilinear coordinate, s. The Green-Lagrange strain tensor is then approximated by

$$\tilde{\mathbf{E}} \approx \frac{R_0}{R_0 - Y_2} \begin{bmatrix} \epsilon - Y_2\kappa & \frac{\gamma}{2} \\ \\ \frac{\gamma}{2} & 0 \end{bmatrix} \tag{B.6}$$

where Y_2 is the coordinate in the $\mathbf{n}$ direction in the reference configuration and

$$\text{Scalar Measure of Stretch}, \epsilon = (1 + e)\cos\alpha - 1, \tag{B.7}$$

$$\text{Scalar Measure of Shear}, \gamma = (1 + e)\sin\alpha, \tag{B.8}$$

$$\text{Scalar Measure of Bending Deformation}, \kappa = \phi' - \phi_0' \tag{B.9}$$

R_0 is the initial radius of curvature of the beam given by $R_0 = \frac{1}{\phi_0'}$. See Appendix A for the full derivation of the Green-Lagrange strain tensor approximation as shown by [?].

Using the theorem of virtual work,

$$\delta W_{int} - \delta W_{ext} = 0 \tag{B.10}$$

where

$$\delta W_{int} = \int_0^{L_0} (P\delta\epsilon + V\delta\gamma + M\delta\kappa)ds \tag{B.11}$$

and

$$\delta W_{ext} = \int_0^{L_0} (\boldsymbol{p} \cdot \delta \boldsymbol{u} + \mu \delta \phi) ds + \sum_{j=1}^{N} [\boldsymbol{f}^j \cdot \delta \boldsymbol{u} + m^j \delta \phi]_{s=s^j} \tag{B.12}$$

These kinematics were then used along with the theorem of virtual work to arrive at three nonlinear ordinary differential equations describing the equilibrium of the system:

$$\left\{ \begin{array}{c} (\mathbf{R} \cdot \mathbf{\Xi})' = \mathbf{p} \\ \mathbf{M}' - \mathrm{e} : (\mathbf{\Xi} \otimes \mathbf{\Pi}) = \mu \end{array} \right\} \tag{B.13}$$

where $\mathbf{\Xi}$ is the measure of axial shear stress, $\mathbf{\Pi}$ is the measure of axial strain:

$$\mathbf{\Xi} = \begin{bmatrix} P \\ V \end{bmatrix} \qquad \text{and} \qquad \mathbf{\Pi} = \begin{bmatrix} \epsilon + 1 \\ \gamma \end{bmatrix} \tag{B.14}$$

P, V, and M are the resultants of axial stress, shear stress, and bending moment with respect to the initial configuration, R is the orthogonal rotation matrix, and e is the permutation tensor. The quantities $\mathbf{p}$ and μ are the rectangular components of the applied distributed force and moment resultants, respectively, along the beam.

The boundary conditions at discrete points along the beam are then described as

$$\left\{ \begin{array}{c} [\mathbf{R} \cdot \mathbf{\Xi}](\mathbf{s^j}) = \mathbf{f^j} \\ [M](s^j) = m^j \end{array} \right\} j = 1, ..., q \text{ and} \tag{B.15}$$

$$\left\{ \begin{array}{c} \boldsymbol{u}(s^j) = \bar{\mathbf{u}}^j \\ \phi(s^j) = \bar{\phi}^j \end{array} \right\} j = (q+1), ..., (q+r) \tag{B.16}$$

where q and r denote the number of points at which a concentrated force or moment, or a prescribed displacement or rotation are applied, respectively.

The constitutive equation is yet another vital piece to Vernerey and Pak's theory [17], and is given as a hyperelastic potential, $\Psi(\epsilon, \gamma, \kappa)$, which is related to the stress resulant by

$$[P \ V \ M] = [\Psi_{,\epsilon} \ \Psi_{,\gamma} \ \Psi_{,\kappa}] \tag{B.17}$$

The elastic potential Ψ is written as

$$\Psi(\epsilon, \gamma, \kappa) = \frac{EA}{2} \epsilon^2 + \frac{kGA}{2} \gamma^2 + \frac{EI}{2} \kappa^2 \tag{B.18}$$

Here, E and G are Young's and shear moduli, A and I are the area and the moment of inertia of the cross section, and k is the shape factor representing the effective shear modulus of the beam to allow for nonuniform cross-sectional shear stress distribution.

These equations can then be reduced to define the current coordinate of the beam centroid as

$$\boldsymbol{x}(s) = \boldsymbol{x}(s_0) + \int_{s_0}^{s} \boldsymbol{q}(\boldsymbol{F}, \phi) ds \tag{B.19}$$

where

$$\boldsymbol{q}(\boldsymbol{F}, \phi) = (1 + e) \begin{bmatrix} \cos\beta \\ \sin\beta \end{bmatrix} = \boldsymbol{R} \cdot \boldsymbol{\Pi} = \boldsymbol{w} + \boldsymbol{P}_2 \cdot \boldsymbol{F} \tag{B.20}$$

and

$$\boldsymbol{w}(\phi) = \begin{bmatrix} \cos\phi \\ \sin\phi \end{bmatrix}, \qquad \boldsymbol{F} = \sum_{j=0}^{\eta(s)} \boldsymbol{f}^j(s^j) + \int_0^s \boldsymbol{p}(s) ds, \tag{B.21}$$

$$\eta = \begin{cases} 0 & \text{if} \quad s < s_1 \\ j & \text{if} \quad s \in [s^j, s_{j+1}) \\ N & \text{if} \quad s \geq s_N \end{cases} \tag{B.22}$$

and

$$\boldsymbol{P}_2 = \begin{bmatrix} \lambda_2 + \lambda_1 \cos 2\phi & \lambda_1 \sin 2\phi \\ \lambda_1 \sin 2\phi & \lambda_2 - \lambda_1 \cos 2\phi \end{bmatrix}, \qquad \lambda_1 = \frac{1}{2}\left(\frac{1}{EA} - \frac{1}{kGA}\right), \qquad \lambda_2 = \frac{1}{2}\left(\frac{1}{EA} + \frac{1}{kGA}\right) \tag{B.23}$$

where $\boldsymbol{F}$ is related to the axial stress through $\boldsymbol{\Xi} = \boldsymbol{R}^T \cdot \boldsymbol{F}$ and η is an integer function related to the total number of concentrated forces along the beam, N.

Vernerey and Pak [17] then go on to generalize this reduced formulation such that a variety of kinematic constraints can be applied to the beam. In their paper, they consider only two cases: one in which a prescribed displacement $\bar{\boldsymbol{u}}$ is imposed along a beam, and the second is cross-link

constraint in which two interacting beams are constrained to have the same displacement at their intersection.

For the case of the specified displacement $\bar{\boldsymbol{u}}$ at $s = s^j$, the coordinate of the displacement is given as

$$\boldsymbol{x}(s^j) = \bar{\boldsymbol{x}}^j = \boldsymbol{X}(s^j) + \bar{\boldsymbol{u}} \tag{B.24}$$

An integral equation for $\boldsymbol{f}^j$ is then obtained by using Equation B.19:

$$\int_0^{s^j} \boldsymbol{q}[\boldsymbol{F}(\boldsymbol{f}^j, \phi)]ds = \bar{\boldsymbol{x}}^j - \boldsymbol{x}(0) \tag{B.25}$$

The task is then to find a force $\boldsymbol{f}^j$ such that Equation B.25 is verified. This is accomplished through the use of a finite element method. Similarly, the cross-link constraint equation is given as

$$\int_0^{s_A^j} \boldsymbol{q}[\phi_A, \boldsymbol{F}_A(\boldsymbol{f}^j)]ds - \int_0^{s_b^j} \boldsymbol{q}[\phi_B, \boldsymbol{F}_B(-\boldsymbol{f}^j)]ds = \boldsymbol{x_B}(0) - \boldsymbol{x_A}(0) \tag{B.26}$$

where the subscripts A and B are used to denote quantities related to the beams in question - A and B, and $\boldsymbol{x_B}(0)$ and $\boldsymbol{x_A}(0)$ describe the initial coordinates of the beams.The task is then again to use a finite element method to find a force $\boldsymbol{f}^j$ such that Equation B.26 is verified.

The last step of this derivation is to summarize the reduced beam formulation with the translational constraints. If we consider the case in which the beam is subjected to the load case as described in Equation B.21, the problem consists of finding the orientation of the beam, $\phi(s)$, and the forces $\boldsymbol{f}^j$ through the use of the following three, coupled equations:

$$EI(\phi' - \phi'_0) + g(\boldsymbol{F}, \phi) = 0 \quad \text{on}(0, L) - s^j \tag{B.27}$$

$$\int_0^{s^j} \boldsymbol{q}(\phi, \boldsymbol{F}(\boldsymbol{f}^j))ds = \bar{\boldsymbol{x}}^j - bmx(0) \tag{B.28}$$

$$\int_0^{s_A^j} \boldsymbol{q}[\phi_A, \boldsymbol{F}_A(\boldsymbol{f}^j)]ds - \int_0^{s_b^j} \boldsymbol{q}[\phi_B, \boldsymbol{F}_B(-\boldsymbol{f}^j)]ds = \boldsymbol{x_B}(0) - \boldsymbol{x_A}(0) \tag{B.29}$$

Here, Equation B.27 is the moment equation, B.28 describes the fixed displacement constraint at $s = s^j$, and B.29 describes the cross-link displacement constraint at $s = s_A^j$ and $s = s_B^j$. Additional equations can be used to describe concentrated moments (B.30), fixed rotation constraints (B.31), or cross-link rotation constraints (B.32):

$$EI(\phi' - \phi_0')(s^j) = \bar{M}^j \tag{B.30}$$

$$\phi(s^j) = \bar{\phi}^j \tag{B.31}$$

$$\phi(s_A^j) = \phi(s_B^j) \tag{B.32}$$

B.2   Flexure of Composite Beam

B.2.1   Flexural Stiffness of Foam Specimen

The flexural stiffness of the anisotropic, open-celled, polyurethane foam specimen ($153.39\pm.01$ mm x $167.87\pm.01$ mm x $11.99\pm.01$ mm) was computed using the method of transformed cross-sections, as shown in Figure B.2, where n is defined as $n = \frac{E_c}{E_t}$ and $E_c = .02$MPa and $E_t = .06$MPa are the compressive and tensile moduli of the foam, respectively. The neutral axis in the foam
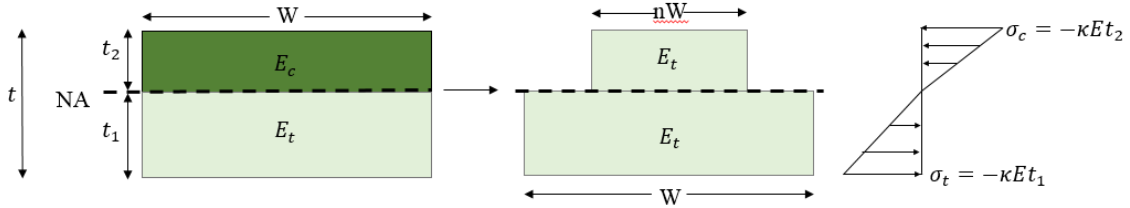
Figure B.2: Diagram of transformed cross-section method for flexural stiffness of foam specimen was determined by equating the resultant compressive and tensile forces generated during flexure:

$$-\frac{\kappa E_c t_2^2}{2} = -\frac{\kappa E_t t_1^2}{2} \tag{B.33}$$

giving

$$NA = \frac{t}{\sqrt{\frac{1}{n} + 1}} \tag{B.34}$$

With these results, the moment of inertia of the foam about the lateral axis (abdomen to dorsal side) is given as

$$I_f = \frac{W(NA)^3}{3} + \frac{nW(t - NA)^3}{3} \tag{B.35}$$

and the flexural stiffness of the foam is then calculated as $E_t I_f$. Since the measured quantities during testing were load and deflection, rather than load and curvature, the appropriate geometric and constitutive equations were employed to convert total curvature to the deflection of the specimen at the midpoint. Using the classic Timoshenko linear elastic beam theory, the curvature, κ for every point along the beam is given by solving

$$M(x) = -E_t I_f \left(\frac{d\theta}{dx}\right) = -E_t I_f \kappa \tag{B.36}$$

where $M(x) = -Px/2$ as given by simple structural analysis of a point load applied to the center of a simply supported beam. Using a finite difference method, and boundary conditions specified to allow the movement of the beam ends in the x-direction and rotation in the y-direction, while restricting their vertical deflection in the y-direction (see Figure A.3), the rotation at every point on the beam was found. Exact formulation of this method can be found in Appendix A. The following equations were then implemented to calculate the new (after deflection) X and Y coordinates of every point on the beam:

$$X(x) = \int_0^{L/2} (1 + \epsilon(x)) \cos\theta(x) dx \tag{B.37}$$

$$Y(x) = \int_0^{L/2} (1 + \epsilon(x)) \sin\theta(x) dx \tag{B.38}$$

Where $\epsilon(x)$ is the axial strain in the foam calculated by

$$\epsilon(x) = \frac{\sigma(x)}{E_f}; \ \sigma(x) = \frac{N(x)}{A} \tag{B.39}$$

and $N(x)$ is calculated as shown in Figure B.3. It was assumed that the axial load was resisted entirely by the foam substrate, and that deformation from shear was negligible since the foam was relatively thin with respect to its length. With each incrementally applied load, the moment equation from a structural analysis was updated, and the solid green curve in Figure 3.1 was generated.
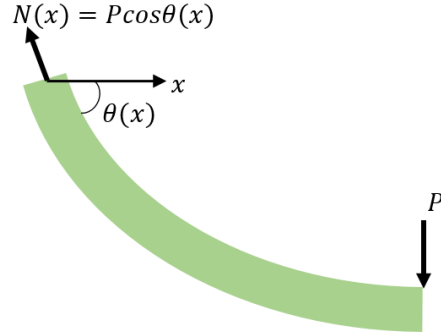
$$N(x) = Pcos\theta(x)$$

Figure B.3: Free-body diagram for calculating beam deformation

B.2.2   Flexural Stiffness of Specimen About the Longitudinal Axis

To the best knowledge of the author, no exact solution exists for the flexural response of fish skin to the moment applied about the longitudinal axis, in part because natural fish skin is not subjected to such modes of deformation. What is proposed here is that the flexural response of the synthetic fish skin in this direction can be modeled as a composite beam with a solid CAB layer having an effective thickness of 3.2 mm, which is calculated by dividing the total volume of scales used in the specimen by the area which they cover during testing:

$$T_{eff} = \frac{n_s h b l}{WL} \tag{B.40}$$

where n_s is the total number scales in the specimen (690), h, b, and l are the thickness, width and length of an individual scale, respectively. W and L are the width and length of the foam specimen that the synthetic skin covered during testing.

Since the synthetic skin was not perfectly adhered to the foam, the internal moment of the specimen is calculated as the sum of the moments generated by the scales and the foam:

$$M(x) = E_t I_f \kappa_f + E_s I_s \kappa_s \tag{B.41}$$

where $E_t I_f$ is the flexural stiffness of the foam as calculated above, E_s is the modulus of elasticity of the CAB (800 MPa), and I_s is the moment of inertia of the scales given as $I_s = \frac{L(T_{eff})^3}{12}$. For the sake of reducing this equation, the curvature of the foam can be related to the curvature of the

scales through the following equation

$$\kappa_f = \frac{1}{\frac{1}{\kappa_s} + .5T_{eff} + (t - NA)} \tag{B.42}$$

With this, it was possible to solve for the curvature of the scales, κ_s, and then use the relation described in the previous section to solve for the deflection of the beam.

B.2.3 Flexural Stiffness of Specimen About the Lateral Axis

Vernerey and Barthelat [19], decomposed the energy associated with fish skin curvature into rotational and bending energies. The rotational energy is described as the energy stored by the skin "pockets" as scales rotate about the lateral axis [19]. The pockets act as springs, resisting out of plane deformation, and as the "springs" are stretched, energy is stored. Scale rotation occurs as the skin first begins to bend, allowing relatively large flexural deformation for a given moment. As the curvature increases, individual scales begin to bend, causing a stiffening in the flexural moment response. Individual scales store this component of the bending energy. These two mechanisms combine to create the overall flexural response in fish skin, as shown in Figure B.4.

By considering the fact that the energy in a structure is equal to the sum of the stored energy in each component of the structure, and then invoking the principle of energy minimization, Vernerey and Barthelat [19] derived that the internal moment can be computed as

$$M = \frac{(EI)_s}{rl} \left(\bar{\kappa} - \bar{\kappa}_r(\bar{\kappa}) \right) \tag{B.43}$$

where EI_s is the bending stiffness of the scales, r and l are the geometric parameters as seen in Figure B.4, and $\bar{\kappa}$ and $\bar{\kappa}_r$ are the normalized total curvature and the curvature generated by scale rotation, respectively. These curvatures are normalized by the length of a single scale, l (e.g. $\bar{\kappa} = l\kappa$) For the full derivation of Equation B.43, see *Skin and scales of teleost fish: simple structure but high performance and multiple functions*[19].

Here, this derivation is combined with a general large deformation bending model (see Equation B.44) for a composite beam composed of an upper scaled layer and a lower polyurethane foam
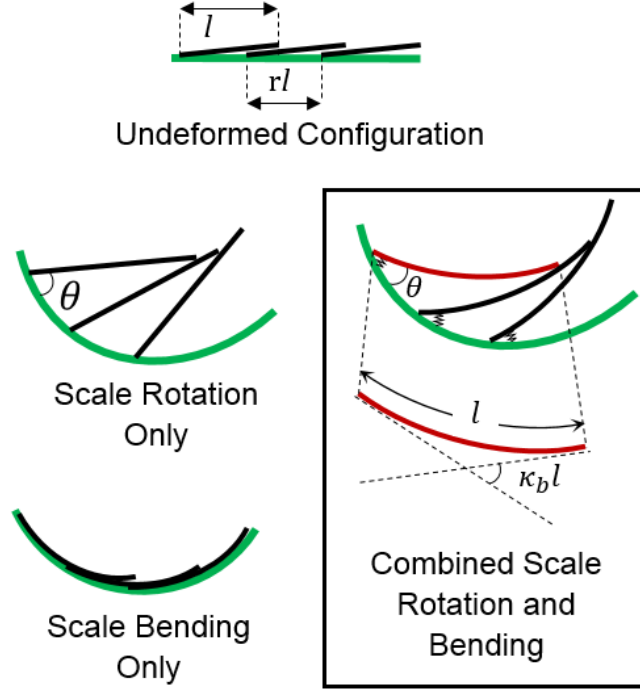
Figure B.4: Illustration of the decomposition of the rotation and scale flexure mechanisms contributing to the overall response of the fish skin

layer. The flexural stiffness associated with the polyurethane foam was computed as described in section 4.3.1. The total external moment generated by the applied load was considered to be equal to the sum of the internal moments of the scales and the foam:

$$M(x) = E_t I_f \bar{\kappa}_f + \frac{(EI)_s}{rl} \left(\bar{\kappa} - \bar{\kappa}_r(\bar{\kappa}) \right) \tag{B.44}$$

where

$$\bar{\kappa}_f = \frac{1}{\left(\frac{1}{\bar{\kappa}}\right) + (t - NA)} \tag{B.45}$$

is the curvature of the foam about the neutral axis, computed with respect to the curvature of the scales and $E_t I_f$ is the flexural stiffness of the foam. In order to solve this equation, the first step is to show with a simple structural analysis that

$$M(x) = \frac{Px}{2} \tag{B.46}$$

Substituting the following equation from Vernerey and Barthelats [19] derivation, we can

simplify this expression further:

$$\bar{\kappa} = \bar{\kappa}_r + \bar{K}\theta(\bar{\kappa}_r)\theta'(\bar{\kappa}_r) \tag{B.47}$$

Transforming Equation B.44 into

$$EI_f\left(\frac{1}{\left(\frac{1}{\bar{\kappa}_r + \bar{K}\theta(\bar{\kappa}_r)\theta'(\bar{\kappa}_r)}\right) + (t - NA)}\right) + \frac{(EI)_s}{rl}\left(\bar{\kappa}_r + \bar{K}\theta(\bar{\kappa}_r)\theta'(\bar{\kappa}_r)\right) - \frac{Px}{2} = 0 \tag{B.48}$$

Where

$$\theta(\bar{\kappa}_r) = \frac{-r\bar{\kappa}_r}{2} + \sin^1(\bar{\kappa}_r \cos(\frac{r\bar{\kappa}_r}{2})) \tag{B.49}$$

and

$$\theta'(\bar{\kappa}_r) = \frac{-r}{2} + \frac{\cos(\frac{r\bar{\kappa}_r}{2}) - \frac{r\bar{\kappa}_r}{2}\sin(\frac{r\bar{\kappa}_r}{2})}{\sqrt{1 - (\bar{\kappa}_r \cos(\frac{r\bar{\kappa}_r}{2}))^2}} \tag{B.50}$$

The normalized rotational curvature can be found through the use of a Newton-Raphson algorithm, and in turn, the total normalized curvature can be found using Equation B.47. This quantity is then transformed into the actual curvature by dividing by the length of a scale l. Once the value for curvature at every point along the beam was determined, the relations described in Section 4.3.1 were used to determine the deflection of the beam.

Appendix C 3-pt Bending Model Matlab Code

```matlab
clear all; close all; clc
%Set-up Problem Material Parameters
Thickness=(13.78+10.39+10.76+14.86+11.38)/5;
t=.98*Thickness/1000;
L=167.87/1000;
L2=153.39/1000;
Et=.059567*10^6; %MPa tensile modulus of foam
Ec=.023*10^6; %compressive modulus of foam
bw=9.46/1000; l=12.68/1000; h=.2/1000; rl=2.35/1000; r=rl/l; ro=r;
stiff=.1; %Stiffness of scale pocket Es=800*10^6; %Elastic modulus of scales
%************************************************************%
%%********************MODEL****************************%%
%%%*********************************************************%%%
Is=L2*(2*h)^3/12; %Moment of Inertia of scale layer EIs=Es*Is; %Flexural Stiffness of Scales
K=stiff*l/EIs; %Normalized Pocket Stiffness

%Foam Transformed Section Method
nf=Ec/Et; NA=t/(sqrt(1/nf)+1); Iz1f=L2*(NA)^3/3;
Iz2f=nf*L2*(t-NA)^3/3; Isolidf=Iz1f+Iz2f;

%Transformed foam for lateral
NAl=.8*t; Iz2fl=L*NAl^3/3; Iz3fl=nf*L*(t-NAl)^3/3;
solidfl=Iz2fl+Iz3fl;

%Solid CAB
T1=h; funNA=@ (NAc) h*(3*Es*(t-NAc)+4*Es*h+Ec*(t-NAc))+Ec*(t-NAc)^2-Et*NAc^2; NAc=fsolve(funNA, .0001);
Isolidfc=L2*t^3/12+L2*t*(NAc-.5*t)^2; Iz1=L2*h^3/12+L2*h*(abs((t+h*.5)-NAc))^2; Iz2=L2*h^3/12+L2*h*((t+1.5*h)-
NAc)^2;
%%Bending About Long Axis Trans. Section
nscales=690; %Used to determine scale density and actual effective % thickness of scales if they were consolidated to a
single sheet
tt=nscales*h*bw*l/(1*L2*L); Iz1s=L*tt^3/12; %Scales

%Set-up problem to solve for M, kappa, and displacement at every point on %beam
dx=.001; %dx
 x=0:dx:L/2; %x vector
x=x'; P=0:.1:1; %Line load, P
iter=0;wmax=[];Xff=x; Xffoam=x; Xffsol=x; Xffsoll=x;
for k=1:length(P)
      iter=iter+1
      Ms(:,k)=.5*P(k)*(Xff); %Moment, M(x) -changes after each load increment
      Msf(:,k)=.5*P(k)*(Xffoam);
       Msol(:,k)=.5*P(k)*(Xffsol);
      Msoll(:,k)=.5*P(k)*Xffsoll;
      for i=1:length(x)
%====================About Lateral Axis====================
              theta1=@(k r) (-r*k r/2)+asin(k r*cos(r*k r/2)); thetap=@(k r)(-r/2)+(cos(r*k r/2)-.5*r*k r*sin(r*k
              r/2))/sqrt(1-((k r*cos(r*k r/2))^2)); fun=@(k r) -Ms(i,k)+Et*Isolidf*(1/((1/(k r+K*theta1(k r)*thetap(k
              r)))+(t-NA)))+...
                    (EIs/(r*l))*(K*theta1(k r)*thetap(k r)); k r=fsolve(fun,.001); kr(i,k)=k r;
              kappa(i,k)=(kr(i,k)+K*theta1(kr(i,k))*thetap(kr(i,k)))/(l);
                kappa(i,k)=kr(i,k)+K*((-r*kr(i,k)/2)+asin(kr(i,k)*cos(r*kr(i,k)/2)))*((-r/2)+... (cos(r*kr(i,k)/2)-
                (.5*r*kr(i,k)*sin(r*kr(i,k)*.5)))/sqrt(1-(kr(i,k)*cos(r*kr(i,k)/2))^2));
%====================Foam Only====================
            kappaf(i,k)=Msf(i,k)/(Et*Isolidf);
%================Solid CAB================
```

```
                    funfun=@ (ks) -Msol(i,k)+Et*Isolidfc*ks+Es*Iz1*ks+Es*Iz2*ks; ks=fsolve(funfun,.001); kappa solid(i,k)=ks;
%=============About Longitudinal Axis===============
                    unfun=@ (ksl) -Msoll(i,k)+Et*Isolidf*(1/((1/ksl)+.5*tt+(t-NA)))+Es*Iz1s*ksl; ksl=fsolve(unfun,.001);
                    kappalat(i,k)=ksl;
          end
%***********************************************************************
 %*************** Set up Finite Difference Model **********************
%***********************************************************************
%Solve for theta(x) of scaled system %a,b,c vectors
J=length(x); a1 = 0; b1 = -1/dx; c1 = 1/dx; aJ = 0; bJ = -1/dx; cJ = 1/dx; a=[a1;(0)*ones(J-2,1);aJ]; b=[b1;(-1/(dx))*ones(J-
2,1);bJ]; c=[c1;(1/(dx))*ones(J-2,1);cJ];
theta(:,k)=thomas(a,b,c,kappa(:,k));
          %Solve for axial stress/strain
                    N(:,k)=P(k)*cos(theta(:,k)); sigma(:,k)=N(:,k)./(L2*(t)); epsilonaxial(:,k)=sigma(:,k)./(Et);
%Solve for theta(x) of non-scaled system %a,b,c vectors
Jf=length(x); a1f = 0; b1f = -1/dx; c1f = 1/dx; aJf = 0; bJf = -1/dx; cJf = 1/dx; af=[a1f; 0*ones(Jf-2,1);aJf]; bf=[b1f;(-
1/(dx))*ones(Jf-2,1);bJf]; cf=[c1f;(1/(dx))*ones(Jf-2,1);cJf];
thetaf(:,k)=thomas(af,bf,cf,kappaf(:,k));
%Solve for theta(x) of solid system %a,b,c vectors
Js=length(x); a1s = 0; b1s = -1/dx; c1s = 1/dx; aJs = 0; bJs = -1/dx; cJs = 1/dx;
as=[a1s;(0)*ones(Js-2,1);aJs]; bs=[b1s;(-1/(dx))*ones(Js-2,1);bJs]; cs=[c1s;(1/(dx))*ones(Js-2,1);cJs];
theta solid(:,k)=thomas(as,bs,cs,kappa solid(:,k));
%Solve for theta(x) of lateral system %a,b,c vectors
Jsl=length(x); a1sl = 0; b1sl = -1/dx; c1sl = 1/dx; aJsl = 0; bJsl = -1/dx; cJsl = 1/dx; asl=[a1sl;(0)*ones(Jsl-2,1);aJsl];
bsl=[b1sl;(-1/(dx))*ones(Jsl-2,1);bJsl]; csl=[c1sl;(1/(dx))*ones(Jsl-2,1);cJsl];
thetalat(:,k)=thomas(asl,bsl,csl,kappalat(:,k));
%***************Non-Linear Beam Theory***************
X(1,k)=0; y(1,k)=0;%Scales Xsol(1,k)=0; ysol(1,k)=0;%Solid Xsoll(1,k)=0;
ysoll(1,k)=0;%Lateral Xf(1,k)=0; yf(1,k)=0;%No Scales
          for i=2:length(x)
                    %Scales
                    X(i,k)=X(i-1,k)+dx*(1+epsilonaxial(i,k))*cos(theta(i,k)); y(i,k)=y(i-
                    1,k)+dx*(1+epsilonaxial(i,k))*sin(theta(i,k));
                    %No Scales
                    Xf(i,k)=Xf(i-1,k)+dx*cos(thetaf(i,k)); yf(i,k)=yf(i-1,k)+dx*sin(thetaf(i,k));
                    %Solid
                    Xsol(i,k)=Xsol(i-1,k)+dx*cos(theta solid(i,k)); ysol(i,k)=ysol(i-1,k)+dx*sin(theta solid(i,k));
                    %Lateral
                    Xsoll(i,k)=Xsoll(i-1,k)+dx*cos(thetalat(i,k)); ysoll(i,k)=ysoll(i-1,k)+dx*sin(thetalat(i,k));
          end
          Xffoam=Xf(:,k); Xff=X(:,k); Xffsol=Xsol(:,k);
          Xffsoll=Xsoll(:,k);
end
f=EIs*(kappa-kr); ymax=max(abs(y)); %Deflection at midpoint with scales ymaxf=max(abs(yf)); %Deflection at midpoint
without scales ymaxsol=max(abs(ysol)); ymaxsoll=max(abs(ysoll)); figure; plot(x,laterror)
%Plot Deflected Shape
figure; plot(X,y,'b') hold on plot(Xf,yf,'r') legend('P=0','P=.1','P=.2','P=.3','P=.4','P=.5','P=.6','P=.7','P=.8','P=.9','P=1')
xlabel('x', 'FontSize',12) ylabel('y', 'FontSize',12) legend('With Scales','Without Scales')
%Plot delta vs. P
figure; plot(ymax',P,'r','LineWidth',2) %Scales hold on plot(ymaxf',P,'Color',[0 .8 0],'LineWidth',2) %No Scales Without
Stretch hold on plot(ymaxsol',P,'k','LineWidth',2) %Solid hold on plot(ymaxsoll',P,'b','LineWidth',2) %Lateral %%Real
Data about Lateral Axis with scales
          F1=[0 0.098 0.196 0.294 0.392 0.49 0.588 0.686 0.784 0.882 0.98]; Delta1=[0 0.00542 0.01077 0.01382 0.01591
          0.01947 0.02186 0.026163333 0.02984 0.03263 0.0355];
%%Real Data about Lateral Axis without Scales
          F=[0 0.098 0.196 0.294 0.392 0.49 0.588 0.686 0.784 0.882 0.98]; Delta=[0 18.61 29.15 35.08 38.64 43.75 48.34
          52.48 54.48 57.03 58.81]./1000;
%%Real Data for solid sheet
          Fsol=[0 0.098 0.196 0.294 0.392 0.49 0.588 0.686 0.784 0.882 0.98]; Deltasol=[0 0.94 3.61 5.23 8.1 11.51 12.16
          13.69 15.25 17.59 21.28]./1000;
%%Real Data for Long
          Fsoll=Fsol;
          Deltasoll=[0 0.0035 0.00691 0.00825 0.01154 0.0133 0.01545 0.01726 0.01933 0.02229 0.02323]; hold on
```

```matlab
plot(Deltasoll,Fsoll,'b^','MarkerSize',10) hold on plot(Delta,F,'*','Color',[0 .8 0],'MarkerSize',10) hold on
plot(Delta1,F1,'ro','MarkerSize',10) hold on plot(Deltasol,Fsol,'k^','MarkerSize',10)
% legend('Model of Solid CAB-2 Sheets','Model of Scales', 'Experimental data for scales', 'Experimental %
xlabel('Deflection at x=L/2, m', 'FontSize',15) % ylabel('Force, N', 'FontSize',15)
```